

# Fibonacci-Modulation-Induced Multiple Topological Anderson Insulators

Ruijiang Ji<sup>1</sup> and Zhihao Xu<sup>1,2,\*</sup>

<sup>1</sup>*Institute of Theoretical Physics and State Key Laboratory of Quantum Optics and Quantum Optics Devices, Shanxi University, Taiyuan 030006, China*

<sup>2</sup>*Collaborative Innovation Center of Extreme Optics, Shanxi University, Taiyuan 030006, China*

(Dated: January 7, 2025)

We uncover the emergence of multiple topological Anderson insulators (TAIs) in a 1D spin-orbit coupled (SOC) chain driven by Fibonacci modulation, transforming a trivial band structure into a cascade of topologically nontrivial phases. This intriguing phenomenon is marked by the appearance of zero-energy modes and transitions in the  $\mathcal{Z}_2$  topological quantum number. Strikingly, as the SOC amplitude decreases, the number of TAI phases grows, a behavior intricately linked to the fractal structure of the energy spectrum induced by Fibonacci modulation. Unlike conventional TAI phases, which exhibit fully localized eigenstates, the wave functions in the Fibonacci-modulated TAI phases exhibit multifractal behavior. Furthermore, this model can be experimentally realized in a Bose-Einstein condensate along the momentum lattice, where its topological transitions and multifractal properties can be probed through quench dynamics. Our findings open new avenues for exploring exotic disorder-induced topological phases and their intricate multifractal nature.

*Introduction.*—Topological states of matter have been extensively studied in various systems, including condensed-matter materials[1–5], ultracold atoms[6, 7], superconducting circuits[8–11], electronic circuits[12], photonic lattices[13–17], and mechanical systems[18]. Topological insulators are characterized by gapless edge states that are immune to backscattering from weak disorders[19–21], but these states typically cannot survive strong disorders due to Anderson localization[22, 23]. Interestingly, a reverse transition has been observed: disorder can induce the emergence of protected edge states and quantized transport even in a trivial band structure. This disorder-induced topological phase, known as the topological Anderson insulator (TAI)[24–34], has been theoretically predicted in systems such as the two-dimensional (2D) HgTe/CdTe quantum well[24, 25, 35] and the 1D Su-Schrieffer-Heeger chain[36], and experimentally realized in a variety of engineered systems, including 1D cold atomic wires[37], 2D photonic waveguide arrays[38, 39], and photonic quantum walk[40]. Notably, both uncorrelated random[37, 41–46] and quasiperiodic disorders in the form of a cosine modulation incommensurate with lattice spacing[34, 47–51] can give rise to the TAI phase. Expanding the range of disorder types that can induce the TAI phase, and exploring the associated exotic topological and localization effects, remains a critical focus of ongoing research.

Quasicrystals offer intriguing platforms for studying exotic localization phenomena and topologically nontrivial behavior in physics[52–59]. Unlike randomly disordered systems, quasicrystals exhibit a structure that is long-range ordered but not periodic[60, 61]. Significant advancements in quasicrystal growth and synthetic engineering, achieved with atomic and photonic preci-

sion, have made it possible to create quasiperiodic structures. A notable example is the Fibonacci quasicrystal, which hosts critical states that are neither fully localized nor extended[61–67], along with a multifractal spectrum of topological gaps and subgap winding states[56–59]. Synthetic Fibonacci chains have been realized in various contexts, including cold atoms[68, 69], photonics[64, 70–72], polaritonics[73, 74], and dielectric chains or circuits[75, 76], where the wave functions and topological properties of Fibonacci chains have been experimentally measured[56, 77–80].

In this Letter, we report the emergence of multiple topological Anderson insulators (TAIs) induced by Fibonacci modulation in a 1D spin-orbit coupled (SOC) chain, starting from a trivial band structure. This intriguing phenomenon is confirmed by the appearance of nontrivial zero modes, along with changes in the  $\mathcal{Z}_2$  topological quantum number. The number of TAI phases increases as the SOC amplitude decreases. The fractal structure of the spectrum plays a crucial role in governing the emergence of these multiple TAI phases. Specifically, the self-similar splitting of the spectrum induced by the Fibonacci modulation facilitates the formation of multiple topologically nontrivial regions, which evolve as the SOC amplitude is varied. In contrast to conventional TAI phases, which exhibit fully localized eigenstates, the wave functions in the Fibonacci-modulated TAI phases display multifractal characteristics. Furthermore, our model can be experimentally realized in a Bose-Einstein condensate along the momentum lattice, where its topological transitions and multifractal behavior can be probed through quench dynamics.

*Model.*—We study a 1D SOC atomic chain with a Fibonacci-modulated on-site potential, described by the Hamiltonian

$$H = \sum_{\langle i,j \rangle} \Psi_i^\dagger \mathcal{R}_{ij} \Psi_j + \sum_i \Psi_i^\dagger \mathcal{U}_i \Psi_i, \quad (1)$$

\* xuzhihao@sxu.edu.cn

where  $\Psi_i^\dagger = (c_{i\uparrow}^\dagger, c_{i\downarrow}^\dagger)$  with  $c_{i\beta}^\dagger$  creating a particle with spin  $\beta = \{\uparrow, \downarrow\}$  at site  $i$ . The hopping matrix takes the form  $\mathcal{R}_{ij} = -t_0\sigma_z \pm it_{so}\sigma_y$ , along the  $\pm\hat{x}$  direction, respectively. The diagonal terms of  $\mathcal{R}$  describe the spin-conserved hopping with the amplitude  $t_0$  (set to unit,  $t_0 = 1$ ) and its off-diagonal terms represent the spin-flip hopping between the nearest neighbors with the amplitude  $t_{so}$ . The second term in the Hamiltonian corresponds to an on-site Fibonacci modulation  $\mathcal{U}_i = [\lambda \text{sgn}(\cos(2\pi\alpha i + \phi) - \cos(\pi\alpha)) + M]\sigma_z$  [61], where  $M$  denotes a constant uniform Zeeman potential,  $\lambda$  is the amplitude of quasiperiodic modulation,  $\text{sgn}[\dots]$  denotes the sign function, and  $\phi \in [0, 2\pi)$  is an arbitrary phase. The modulation frequency  $\alpha = (\sqrt{5} - 1)/2$  is derived from the Fibonacci sequence  $F_{\nu+1} = F_{\nu-1} + F_\nu$ , with  $F_0 = F_1 = 1$  [81]. We take the rational approximation  $\alpha = F_{\nu-1}/F_\nu$  with the system size chosen as  $L = F_\nu$ .

The Hamiltonian  $H$  respecting the chiral symmetry defined by  $\sigma_x$  in spin space governs a Fibonacci-modulated SOC chain, whose counterpart with a constant uniform Zeeman potential can rise to the 1D AIII class topological insulator [82]. In the crystalline case, where  $\mathcal{U}_i = M\sigma_z$ , the clean SOC model splits into two bands with the eigenvalues  $E_\pm = \pm\sqrt{(M - 2\cos k)^2 + 4t_{so}^2 \sin^2 k}$ , where  $k$  is the wave vector. For  $|M| > 2$ , regardless of whether  $t_{so} \neq 0$ , a topological phase transition occurs, marked by a gap closing at  $|M| = 2$ . This transition is also characterized by the vanishing of zero-energy edge modes and the disappearance of nontrivial topological invariants. The main focus of this Letter is on the topological phase transition and localization effects induced by the Fibonacci modulation.

*TAI and multiple TAIs*—Topologically protected edge states and quantized topological charges emerge in the context of TAI when sufficient disorder or incommensurate modulation is introduced to a trivial band structure. We employ the scattering-matrix method to compute the  $\mathcal{Z}_2$  topological quantum number  $Q$  in our case [83], where  $Q = 1$  ( $Q = -1$ ) corresponds to a topologically trivial (nontrivial) phase. Figure 1(a) shows the disorder-averaged topological phase diagram with  $t_{so} = 0.5$  as a function of  $M$  and  $\lambda$ , obtained numerically averaging the disorder-averaged  $\mathcal{Z}_2$  number  $\overline{Q}$  over  $N_c$  disorder realizations for different  $\phi \in [0, 2\pi)$ . The phase boundaries can be determined by the condition:

$$|\text{Tr}(T)| - \text{Det}(T) = 1, \quad (2)$$

where  $T$  is the total transfer matrix defined in a new basis  $\tilde{\Psi}_i^\dagger = (c_{i\uparrow}^\dagger + c_{i\downarrow}^\dagger, c_{i\uparrow}^\dagger - c_{i\downarrow}^\dagger)$  for the zero modes [83]. In the absence of  $\lambda$ , the system exhibits a topological phase transition at  $|M| = 2$ , corresponding to a jump in  $\overline{Q}$  from  $-1$  to  $1$  as  $|M|$  increases. When the Fibonacci modulation is introduced to the nontrivial band structure with  $|M| < 2$ , the topologically nontrivial phase remains robust against weak  $\lambda$ , but eventually transi-

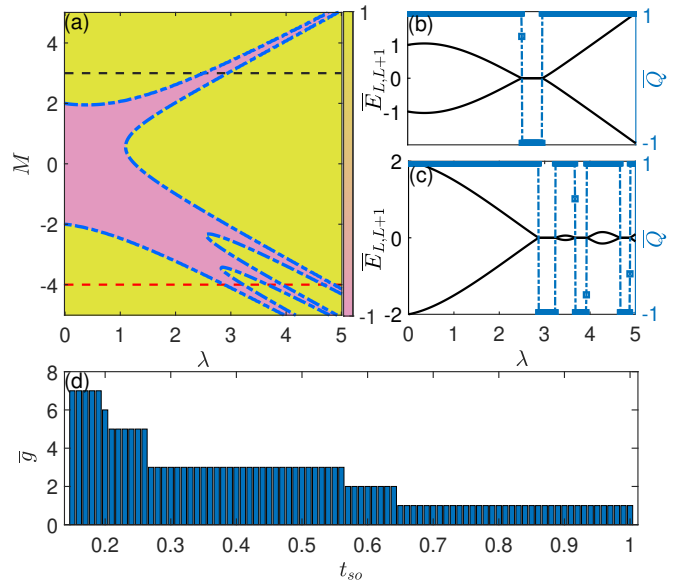


FIG. 1. (Color online) (a) The disorder-averaged topological phase diagram of the system in  $M - \lambda$  plane with  $t_{so} = 0.5$ . The blue dashed lines correspond to the topological phase boundaries determined by Eq.(2). Two disorder-averaged energies  $\overline{E}_L$  and  $\overline{E}_{L+1}$  at the center of the spectrum and the disorder-averaged topological number  $\overline{Q}$  as a function of  $\lambda$  under OBC with  $t_{so} = 0.5$  for (b)  $M = 3$  and (c)  $M = -4$ . (d) The number of times the TAI phases emerge, denoted as  $\overline{g}$ , as a function of  $t_{so}$  with  $M = -4$ . Here, all the data are averaged by  $N_c = 50$  disorder realizations.

tions to a trivial one for sufficiently strong modulation. For  $M > 2$ , the system undergoes a topological phase transition from trivial to nontrivial as  $\lambda$  increases, indicating the emergence of the TAI. We further present two disorder-averaged energies,  $\overline{E}_L$  and  $\overline{E}_{L+1}$ , at the center of the spectrum, as well as  $\overline{Q}$  as a function of  $\lambda$  under open boundary condition (OBC) with  $M = 3$  and  $t_{so} = 0.5$  in Fig. 1(b). When  $\lambda$  lies in the range  $[2.51, 2.94]$ , the topological number  $\overline{Q}$  jumps from  $1$  to  $-1$ , accompanied by the emergence of the zero edge modes. For  $\lambda > 2.94$ , the topologically nontrivial phase vanishes. Our numerical results suggest that the Fibonacci modulation can induce the TAI.

As seen in Fig. 1(a) for  $M < -2$ , the system undergoes multiple distinct transitions into the TAI phase, eventually returning to a trivial phase as  $\lambda$  increases further. Figure 1(c) shows the disorder-averaged energies of the two center modes,  $\overline{E}_L$  and  $\overline{E}_{L+1}$ , as well as  $\overline{Q}$  as a function of  $\lambda$  with  $M = -4$  and  $t_{so} = 0.5$ . It can be observed that, as the  $\mathcal{Z}_2$  number  $\overline{Q}$  transitions to a nontrivial value, corresponding zero modes emerge in the ranges  $\lambda \in (2.87, 3.22) \cup (3.67, 3.94) \cup (4.66, 4.88)$ . The system undergoes three transitions from topologically trivial phases to nontrivial ones, indicating the emergence of the multiple TAI phases. For a given  $M < -2$ , the number of times TAI phases emerge, denoted by  $g$ , strongly de-

pend on  $t_{so}$ . As shown in Fig. 1(d) with  $M = -4$ ,  $\bar{g}$  gradually increases as  $t_{so}$  decreases, for  $N_c = 50$  disorder realizations.

To uncover the underlying mechanism of this phenomenon, we analyze the energy spectrum of two decoupled Fibonacci-modulated chains without the SOC term ( $t_{so} = 0$ ) as described in Eq. (1), shown in Fig. 2(a) for  $\phi = 0$ . For finite  $\lambda$ , the spectrum exhibits eight primary bands. Within the range  $\lambda \in (2.76, 4.95)$ , the middle six bands overlap, forming three clusters of band-crossing regions separated by two prominent band gaps near zero energy. Remarkably, each cluster undergoes successive splitting into smaller sub-clusters, creating a self-similar fractal structure that persists in the thermodynamic limit. This fractal nature manifests in the emergence of progressively smaller band gaps  $\Delta_g$  at each level of splitting. When the SOC strength  $t_{so}$  is introduced, these band gaps—comparable in size to  $t_{so}$ —begin to close and reopen, signaling the formation of nontrivial zero-energy modes, as illustrated in Fig. 2(b). This process unveils an infinite hierarchy of TAI phases in the small  $t_{so}$  regime and in the thermodynamic limit, effectively creating a topologically fractal structure. As  $t_{so}$  increases further, neighboring topologically nontrivial regions merge, reducing the number of distinct TAI phases. This transition, depicted in Figs. 2(c) and 2(d), signifies a transformation from a fractal topology to a more discrete structure, highlighting how the interplay between SOC and Fibonacci modulation reshapes the landscape of topological phases.

We investigate an off-diagonal Fibonacci-modulated SOC chain and uncover the emergence of multiple TAI phases, whose occurrence strongly depends on  $t_{so}$ . Notably, the localization properties exhibit multifractal behavior, regardless of whether the system resides in a TAI phase or not, as detailed in the Supplementary Material [83]. These findings demonstrate that both diagonal and off-diagonal Fibonacci modulation in SOC chains can induce multiple TAI phases, offering new insights into quasiperiodic topological systems.

*Localization properties.*—A commonly held view is that in the TAI phase, all states are localized, exhibiting Anderson localization. However, in our case, the Fibonacci modulation fundamentally alters the localization properties. Nearly all the states demonstrate multifractal characteristics for any nonzero  $\lambda$ , irrespective of the topological phase. Figure 3 shows the density distributions of different eigenstates in distinct topological phases in both real and momentum spaces, respectively. The momentum-space density distribution is defined as  $n_k = 1/L \sum_{i,j} e^{-ik(i-j)} (\rho_{ij}^\uparrow + \rho_{ij}^\downarrow)$ , where  $\rho_{ij}^{(\beta)} = \langle \Psi_n | c_{i\beta}^\dagger c_{j\beta} | \Psi_n \rangle$  represents the single-particle density matrix of the  $n$ th eigenstate  $|\Psi_n\rangle = \sum_{i,\beta} \psi_{i\beta}^{(n)} |i, \beta\rangle$ , with the eigenvalue  $E_n$ . The real-space density distribution is given by  $n_i = \rho_{ii}^{(\uparrow)} + \rho_{ii}^{(\downarrow)}$ . In momentum space,

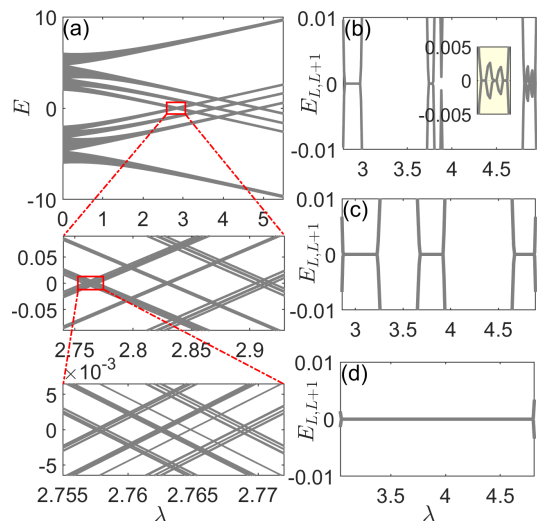


FIG. 2. (Color online) (a) Self-similarities of energy spectrum as a function of  $\lambda$  with  $t_{so} = 0$ . Two central energy levels  $E_L$  and  $E_{L+1}$  as a function of  $\lambda$  with (b)  $t_{so} = 0.25$ , (c) 0.5, and (d) 0.9. Here,  $M = -4$ ,  $\phi = 0$ , and  $L = 610$ .

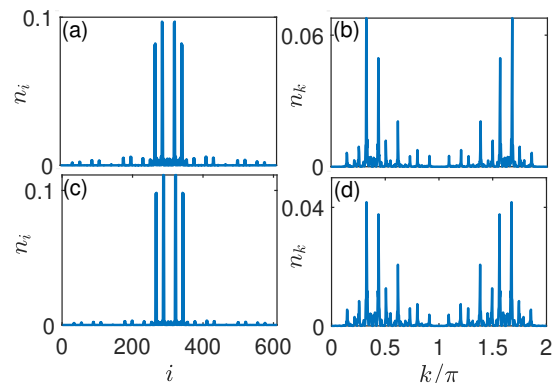


FIG. 3. (Color online) Density distributions of the selected states in both real (the left column) and momentum (the right column) spaces. The top row corresponds to the 198th eigenstates with  $\lambda = 2$ . The bottom row corresponds to the 198th eigenstates with  $\lambda = 3$ . Here,  $t_{so} = 0.5$ ,  $M = -4$ ,  $\phi = 0$ , and  $L = 610$ .

a localized (extended) state exhibits an extended (localized) distribution. Multifractal states, however, exhibit delocalized yet nonergodic behavior in both real and momentum spaces. We select the 198th eigenstates for  $\lambda = 2$  in the topologically trivial phase and  $\lambda = 3$  in the TAI phase with  $L = 610$  and  $\phi = 0$  under OBC, as shown in the top and bottom rows of Fig. 3, respectively. The density distributions in both spaces confirm the multifractal behavior, which persists regardless of whether the states is localized in topologically nontrivial phase or not.

To characterize the localization properties of the wave function, we calculate the fractal dimension of  $n$ th eigenstate using  $D_n = -\lim_{L \rightarrow \infty} \ln(\text{IPR}_n) / \ln(2L)$ , with the inverse participation ratio  $\text{IPR}_n = \sum_{i,\beta} |\psi_{i\beta}^{(n)}|^4$ . For a

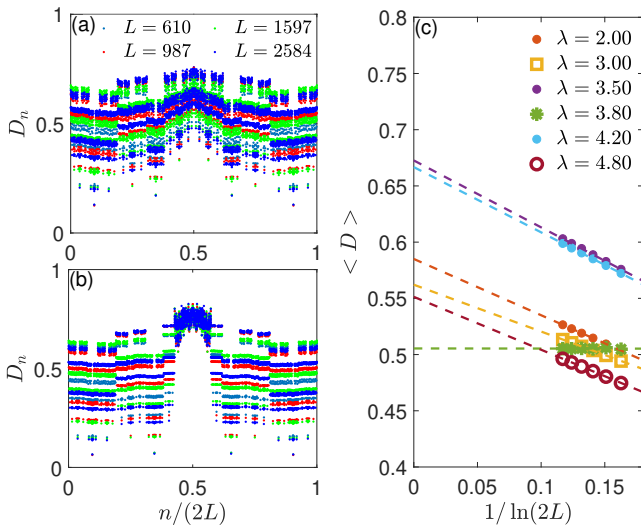


FIG. 4. (Color online) Fractal dimensions  $D_n$  for different system sizes under PBC for (a)  $\lambda = 2$  and (b)  $\lambda = 3$ , respectively. (c) The scaling of the mean fractal dimensions  $\langle D \rangle$  for various  $\lambda$  values. Here,  $t_{so} = 0.5$ ,  $M = -4$ , and  $\phi = 0$ .

localized (extended) state,  $D_n \rightarrow 0$  ( $D_n \rightarrow 1$ ) in the thermodynamic limit. When  $0 < D_n < 1$ , the state is considered multifractal. Figures 4(a) and 4(b) show the fractal dimensions for different system sizes under periodic boundary condition (PBC) with  $\phi = 0$  for  $\lambda = 2$  and  $\lambda = 3$ , respectively. For both topologically trivial and nontrivial phases, the fractal dimensions of nearly all states are system-size independent, deviating from the extremes of 0 and 1. The scaling behavior of the mean fractal dimension  $\langle D \rangle = 1/(2L) \sum_n D_n$  for various  $\lambda$  values, in both topologically trivial ( $\lambda = 2, 3.5$ , and  $4.2$ ) and nontrivial ( $\lambda = 3, 3.8$ , and  $4.8$ ) phases, is shown in Fig. 4(c). In the thermodynamic limit,  $\langle D \rangle$  approaches values that deviate from both 0 and 1 in both phases. Our results suggest that the emergence of the TAI phase does not affect the localization properties of the system, and the states remain multifractal.

*Dynamical detection.*—Experimentally, this Fibonacci-modulated SOC chain can be realized along the momentum lattice [37, 84–94] in a cold atom of Bose-Einstein condensate [83], and its topological properties and localization features can be detected by the quench dynamics. To characterize the topology of our model, we monitor the dynamical response of the system to a sudden quench. Specifically, we measure the mean chiral displacement [34, 37, 42, 51, 95] and the Loschmidt echo (LE) [96–101]. We define the disorder-averaged expectation value of the chiral displacement operator as  $\overline{C}(t) = 2\langle \Psi(t) | \Gamma X | \Psi(t) \rangle$ , where  $\Gamma$  is the chiral operator,  $X$  is the unit cell operator, and  $|\Psi(t)\rangle = e^{iHt} |\Psi(0)\rangle$  is the time-evolved wave function, with the initial state  $|\Psi(0)\rangle = c_{j_0\uparrow}^\dagger |0\rangle$  and  $j_0$  being the position of the central bulk lattice site. The dynamics of  $\overline{C}(t)$  generally

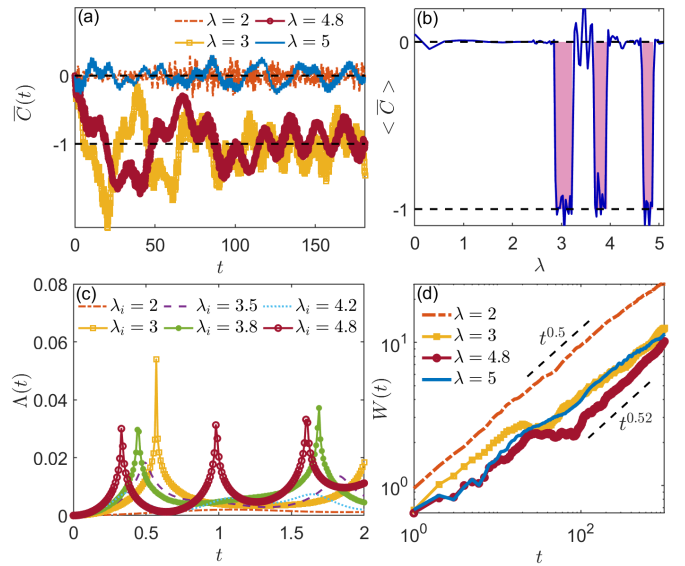


FIG. 5. (Color online) (a)  $\overline{C}(t)$  versus  $t$  for different  $\lambda$  with  $N_c = 50$  disorder realizations. (b)  $\langle \overline{C} \rangle$  as a function of  $\lambda$  with  $N_c = 200$  disorder realizations. (c) The evolution of  $\Lambda(t)$  with  $\lambda_f = 0$ , calculated for the  $(L + 1)$ th eigenstate at different values of  $\lambda_i$  as the initial states. (d) The evolution of  $W(t)$  for different  $\lambda$  with  $\phi = 0$ . Here,  $L = 144$ ,  $t_{so} = 0.5$ , and  $M = -4$ .

exhibit transient, oscillatory behavior, as shown in Fig. 5(a) for different  $\lambda$  with  $M = -4$  and  $t_{so} = 0.5$ . In long time limit,  $\overline{C}(t)$  converges to 0 for  $\lambda$  values corresponding to the topologically trivial phase and to  $-1$  for those corresponding to the nontrivial phase. To eliminate the oscillation, we compute the time average  $\langle \overline{C} \rangle$ , which converges to  $-1$  for a topologically nontrivial phase and to 0 for a trivial one. Figure 5(b) shows  $\langle \overline{C} \rangle$  as the function of the modulation amplitude  $\lambda$  with  $M = -4$  and  $t_{so} = 0.5$ . The value of  $\langle \overline{C} \rangle$  starts at 0, then jumps to a nontrivial value three times, before eventually returning to 0. These results demonstrate that the mean chiral displacement is a sensitive probe of the multiple TAI phases in our model, effectively capturing the topological transitions driven by the modulation amplitude  $\lambda$ .

The LE, defined as  $\mathcal{L}(t) = |\langle \Psi(0) | e^{-iH(\lambda_f)t} | \Psi(0) \rangle|^2$ , is a powerful tool for analyzing nonequilibrium dynamics. It exhibits a series of zero points at specific time intervals when the initial Hamiltonian  $[H(\lambda_i)]$  and the post-quench Hamiltonian  $[H(\lambda_f)]$  describe systems that are localized in different phases. This behavior is a hallmark of dynamical quantum phase transitions (DQPTs), which have been observed in various systems [102–108]. Pioneering studies have established a connection between DQPTs and emergent topological transitions. In particular, dynamical topological order parameters can change their integer values when DQPTs occur, providing a means to dynamically track the topological changes during the quench. The appearance of zero points in the LE

signals the nonanalytic behavior in the dynamical free energy  $\Lambda(t) = -1/(2L)\ln\mathcal{L}(t)$ . Figure 5(c) shows the evolution of  $\Lambda(t)$  with  $\lambda_f = 0$ , calculated for the  $(L+1)$ th eigenstate at different values of  $\lambda_i$  for  $M = -4$  and  $t_{so} = 0.5$  as the initial states. For the topologically trivial Hamiltonian  $H(\lambda_f)$ , when the initial Hamiltonian  $H(\lambda_i)$  is in the topologically nontrivial phase ( $\lambda_i = 3, 3.8,$  and  $4.8$ ), a serial of divergence points of  $\Lambda(t)$ —corresponding to exact zeros of LE—emerge along the time axis. In contrast, for  $\lambda_i$  values within the topologically trivial phase ( $\lambda_i = 2, 3.5,$  and  $4.2$ ), the nonanalytic behavior disappears, indicating that both the initial and the post-quench Hamiltonians are localized in the same topological phase. These results suggest that the LE method not only captures the occurrence of DQPTs but also provides a powerful tool to probe the emergence of multiple TAI phases in our system.

To dynamically detect the localization properties of our system, we employ the mean-square displacement[2, 34, 109, 110] defined as

$$W(t) = \left[ \sum_{j,\beta=\uparrow,\downarrow} (j - j_0)^2 \langle \Psi(t) | c_{j,\beta}^\dagger c_{j,\beta} | \Psi(t) \rangle \right]^{1/2}, \quad (3)$$

where the value of  $W(t)$  grows in a power-law form of time,  $W(t) \propto t^\kappa$ , during the expansion process. Figure 5(d) shows the time evolution of  $W(t)$  for different values of  $\lambda$  in various topological phases, with the initial state  $|\Psi(0)\rangle = c_{j_0\uparrow}^\dagger |0\rangle$  and  $j_0 = L/2 + 1$  for even  $L$ . As seen in Fig. 5(d),  $W(t)$  exhibits subdiffusive behavior with  $\kappa \approx 0.5$ , which corresponds to the multifractal phase. Our results shows that the localization properties in different topological phases remain unchanged, and  $W(t)$  serves as an effective tool to detect these properties.

*Conclusion.*—We have demonstrated that multiple TAI phases can be induced by Fibonacci modulation in a SOC chain. Unlike conventional TAI phases, where the system exhibits full localization, our results show that the system retains multifractal features, regardless of whether it is in the TAI phase or not. Crucially, the emergence of multiple TAI phases is closely tied to the fractal structure of the spectrum induced by the Fibonacci modulation. The self-similar splitting of the bands at each scale enables the formation of multiple TAI phases, resulting in a topologically nontrivial structure that evolves as the SOC amplitude is varied. This model can be experimentally realized along the momentum lattice in a cold atomic system, and its properties can be tested through dynamical evolution experiments.

Z.X. is supported by the NSFC (Grant No. 12375016 and No. 12461160324), and Beijing National Laboratory for Condensed Matter Physics (No. 2023BNL-CMPKF001). This work is also supported by NSF for Shanxi Province (Grant No. 1331KSC).

- 
- [1] M. Z. Hasan, and C. L. Kane, Rev. Mod. Phys. **82**, 3045 (2010).
  - [2] X.-L. Qi, and S.-C. Zhang, Rev. Mod. Phys. **83**, 1057 (2011).
  - [3] A. Bansil, H. Lin, and T. Das, Rev. Mod. Phys. **88**, 021004 (2016).
  - [4] C.-K. Chiu, J. C. Y. Teo, A. P. Schnyder, and S. Ryu, Rev. Mod. Phys. **88**, 035005 (2016).
  - [5] H. Davenport, J. Knolle, and F. Schindler, Phys. Rev. Lett. **133**, 176601 (2024).
  - [6] N. R. Cooper, J. Dalibard, and I. B. Spielman, Rev. Mod. Phys. **91**, 015005 (2019).
  - [7] Z. Jalali-mola, T. Grass, V. Kasper, M. Lewenstein, and U. Bhattacharya, Phys. Rev. Lett. **131**, 226601 (2023).
  - [8] M. D. Schroer, M. H. Kolodrubetz, W. F. Kindel, M. Sandberg, J. Gao, M. R. Vissers, D. P. Pappas, A. Polkovnikov, and K. W. Lehnert, Phys. Rev. Lett. **113**, 050402 (2014).
  - [9] X. Tan, D.-W. Zhang, Z. Yang, J. Chu, Y.-Q. Zhu, D. Li, X. Yang, S. Song, Z. Han, Z. Li, Y. Dong, H.-F. Yu, H. Yan, S.-L. Zhu, and Y. Yu, Phys. Rev. Lett. **122**, 210401 (2019).
  - [10] W. Cai, J. Han, F. Mei, Y. Xu, Y. Ma, X. Li, H. Wang, Y. P. Song, Z.-Y. Xue, Z.-Q. Yin, S. Jia, and L. Sun, Phys. Rev. Lett. **123**, 080501 (2019).
  - [11] X. Tan, D.-W. Zhang, X. Yang, S. Song, Z. Han, Y. Dong, Z. Wang, D. Lan, H. Yan, S.-L. Zhu, and Y. Yu, Phys. Rev. Lett. **126**, 017702 (2021).
  - [12] W. Zhang, D. Zou, Q. Pei, W. He, J. Bao, H. Sun, and X. Zhang, Phys. Rev. Lett. **126**, 146802 (2021).
  - [13] L. Lu, J. D. Joannopoulos, and M. Soljačić, Nat. Photon. **8**, 821 (2014).
  - [14] T. Ozawa, H. M. Price, A. Amo, N. Goldman, M. Hafezi, L. Lu, M. C. Rechtsman, D. Schuster, J. Simon, O. Zilberberg, I. Carusotto, Rev. Mod. Phys. **91**, 015006 (2019).
  - [15] G. Cáceres-Aravena, M. Nedić, P. Vildoso, G. Gligorić, J. Petrovic, A. Maluckov, and R. A. Vicencio, Phys. Rev. Lett. **133**, 116304 (2024).
  - [16] T. Qu, M. Wang, X. Cheng, X. Cui, R.-Y. Zhang, Z.-Q. Zhang, L. Zhang, J. Chen, and C. T. Chan, Phys. Rev. Lett. **132**, 223802 (2024).
  - [17] A. Szameit, and M. C. Rechtsman, Nat. Phys. **20**, 905 (2024).
  - [18] S. D. Huber, Nat. Phys. **12**, 621 (2016).
  - [19] F. D. M. Haldane, and S. Raghu, Phys. Rev. Lett. **100**, 013904 (2008).
  - [20] Z. Wang, Y. D. Chong, J. D. Joannopoulos, and M. Soljačić, Phys. Rev. Lett. **100**, 013905 (2008).
  - [21] Z. Wang, Y. Chong, J. D. Joannopoulos, and M. Soljačić, Nature(London) **461**, 772 (2009).
  - [22] S. Mansha, and Y. D. Chong, Phys. Rev. B **96**, 121405(R) (2017).
  - [23] C. Liu, W. Gao, B. Yang, and S. Zhang, Phys. Rev. Lett. **119**, 183901 (2017).
  - [24] J. Li, R.-L. Chu, J. K. Jain, and S.-Q. Shen, Phys. Rev. Lett. **102**, 136806 (2009).
  - [25] C. W. Groth, M. Wimmer, A. R. Akhmerov, J. Tworzydło, and C. W. J. Beenakker, Phys. Rev. Lett. **103**, 196805 (2009).
  - [26] Y. Xing, L. Zhang, and J. Wang, Phys. Rev. B **84**, 035110 (2011).

- [27] Y.-Y. Zhang, R.-L. Chu, F.-C. Zhang, and S.-Q. Shen, *Phys. Rev. B* **85**, 035107 (2012).
- [28] P. Titum, N. H. Lindner, M. C. Rechtsman, and G. Refael, *Phys. Rev. Lett.* **114**, 056801 (2015).
- [29] C. P. Orth, T. Sekera, C. Bruder, and T. L. Schmidt, *Sci. Rep.* **6**, 24007 (2016).
- [30] Z.-Q. Zhang, B.-L. Wu, J. Song, and H. Jiang, *Phys. Rev. B* **100**, 184202 (2019).
- [31] C. Wang, T. Cheng, Z. Liu, F. Liu, and H. Huang, *Phys. Rev. Lett.* **128**, 056401 (2022).
- [32] X. Cui, R.-Y. Zhang, Z.-Q. Zhang, and C. T. Chan, *Phys. Rev. Lett.* **129**, 043902 (2022).
- [33] M. Ren, Y. Yu, B. Wu, X. Qi, Y. Wang, X. Yao, J. Ren, Z. Guo, H. Jiang, H. Chen, X.-J. Liu, Z. Chen, and Y. Sun, *Phys. Rev. Lett.* **132**, 066602 (2024).
- [34] Z. Lu, Y. Zhang, and Z. Xu, *Front. Phys.* **20**, 024204 (2025).
- [35] H. Jiang, L. Wang, Q.-F. Sun, and X. C. Xie, *Phys. Rev. B* **80**, 165316 (2009).
- [36] A. Altland, D. Bagrets, L. Fritz, A. Kamenev, and H. Schmiedt, *Phys. Rev. Lett.* **112**, 206602 (2014).
- [37] E. J. Meier, F. A. An, A. Dauphin, M. Maffei, P. Massignan, T. L. Hughes, and B. Gadway, *Science* **362**, 929 (2018).
- [38] S. Stützer, Y. Plotnik, Y. Lumer, P. Titum, N. H. Lindner, M. Segev, M. C. Rechtsman, and A. Szameit, *Nature(London)* **560**, 461 (2018).
- [39] G.-G. Liu, Y. Yang, X. Ren, H. Xue, X. Lin, Y.-H. Hu, H.-X. Sun, B. Peng, P. Zhou, Y. Chong, and B. Zhang, *Phys. Rev. Lett.* **125**, 133603 (2020).
- [40] Q. Lin, T. Li, L. Xiao, K. Wang, W. Yi, and P. Xue, *Nat. Commun.* **13**, 3229 (2022).
- [41] D. H. Dunlap, H.-L. Wu, and P. W. Phillips, *Phys. Rev. Lett.* **65**, 88 (1990).
- [42] S.-N. Liu, G.-Q. Zhang, L.-Z. Tang, and D.-W. Zhang, *Phys. Lett. A* **431**, 128004 (2022).
- [43] A. Nava, G. Campagnano, P. Sodano, and D. Giuliano, *Phys. Rev. B* **107**, 035113 (2023).
- [44] E. G. Cinnirella, A. Nava, G. Campagnano, and D. Giuliano, *Phys. Rev. B* **109**, 035114 (2024).
- [45] Z.-W. Zuo, J.-R. Lin, and D. Kang, *Phys. Rev. B* **110**, 085157 (2024).
- [46] A. K. Ghosh, T. Nag, and A. Saha, *Phys. Rev. B* **110**, 125427 (2024).
- [47] G.-Q. Zhang, L.-Z. Tang, L.-F. Zhang, D.-W. Zhang, and S.-L. Zhu, *Phys. Rev. B* **104**, L161118 (2021).
- [48] L.-Z. Tang, S.-N. Liu, G.-Q. Zhang, and D.-W. Zhang, *Phys. Rev. A* **105**, 063327 (2022).
- [49] Z. Lu, Z. Xu, and Y. Zhang, *Ann. Phys.(Berlin)* **534**, 2200203 (2022).
- [50] A. Padhan, S. R. Padhi, and T. Mishra, *Phys. Rev. B* **109**, L020203 (2024).
- [51] X. Li, H. Xu, J. Wang, L.-Z. Tang, D.-W. Zhang, C. Yang, T. Su, C. Wang, Z. Mi, W. Sun, X. Liang, M. Chen, C. Li, Y. Zhang, K. Linghu, J. Han, W. Liu, Y. Feng, P. Liu, G. Xue, J. Zhang, Y. Jin, S.-L. Zhu, H. Yu, S. P. Zhao, and Q.-K. Xue, *Phys. Rev. Res.* **6**, L042038 (2024).
- [52] J. Chabé, G. Lemarié, B. Grémaud, D. Delande, P. Szafranski, and J. C. Garreau, *Phys. Rev. Lett.* **101**, 255702 (2008).
- [53] C. D'Errico, E. Lucioni, L. Tanzi, L. Gori, G. Roux, I. P. McCulloch, T. Giamarchi, M. Inguscio, and G. Modugno, *Phys. Rev. Lett.* **113**, 095301 (2014).
- [54] H. Yao, T. Giamarchi, and L. Sanchez-Palencia, *Phys. Rev. Lett.* **125**, 060401 (2020).
- [55] Q. Dai, Z. Lu, and Z. Xu, *Phys. Rev. B* **108**, 144207 (2023).
- [56] G. Rai, H. Schlömer, C. Matsumura, S. Haas, and A. Jagannathan, *Phys. Rev. B* **104**, 184202 (2021).
- [57] Y. Wang, G. Rai, C. Matsumura, A. Jagannathan, and S. Haas, *Phys. Rev. B* **109**, 214507 (2024).
- [58] A. Kobialka, O. A. Awoga, M. Leijnse, T. Domański, P. Holmval, and A. M. Black-Schaffer, *Phys. Rev. B* **110**, 134508 (2024).
- [59] A. Sandberg, O. A. Awoga, A. M. Black-Schaffer, and P. Holmval, *Phys. Rev. B* **110**, 104513 (2024).
- [60] M. Sbroscia, K. Viebahn, E. Carter, J.-C. Yu, A. Gaunt, and U. Schneider, *Phys. Rev. Lett.* **125**, 200604 (2020).
- [61] A. Jagannathan, *Rev. Mod. Phys.* **93**, 045001 (2021).
- [62] M. Kohmoto, L. P. Kadanoff, and C. Tang, *Phys. Rev. Lett.* **50**, 1870 (1983).
- [63] Y. E. Kraus, and O. Zilberberg, *Phys. Rev. Lett.* **109**, 116404 (2012).
- [64] M. Verbin, O. Zilberberg, Y. E. Kraus, Y. Lahini, and Y. Silberberg, *Phys. Rev. Lett.* **110**, 076403 (2013).
- [65] N. Macé, A. Jagannathan, and F. Piéchon, *Phys. Rev. B* **93**, 205153 (2016).
- [66] N. Macé, A. Jagannathan, P. Kalugin, R. Mosseri, and F. Piéchon, *Phys. Rev. B* **96**, 045138 (2017).
- [67] J.-Q. Liu, and X.-B. Bian, *Phys. Rev. Lett.* **127**, 213901 (2021).
- [68] K. Singh, K. Saha, S. A. Parameswaran, and D. M. Weld, *Phys. Rev. A* **92**, 063426 (2015).
- [69] T. Shimasaki, Y. Bai, H. E. Kondakci, P. Dotti, J. E. Pagett, A. R. Dardia, M. Prichard, A. Eckardt, and D. M. Weld, *Phys. Rev. Lett.* **133**, 083405 (2024).
- [70] L. Dal Negro, C. J. Oton, Z. Gaburro, L. Pavesi, P. Johnson, A. Lagendijk, R. Righini, M. Colocci, and D. S. Wiersma, *Phys. Rev. Lett.* **90**, 055501 (2003).
- [71] Y. E. Kraus, Y. Lahini, Z. Ringel, M. Verbin, and O. Zilberberg, *Phys. Rev. Lett.* **109**, 106402 (2012).
- [72] M. Verbin, O. Zilberberg, Y. Lahini, Y. E. Kraus, and Y. Silberberg, *Phys. Rev. B* **91**, 064201 (2015).
- [73] D. Tanese, E. Gurevich, F. Baboux, T. Jacqmin, A. Lemaitre, E. Galopin, I. Sagnes, A. Amo, J. Bloch, and E. Akkermans, *Phys. Rev. Lett.* **112**, 146404 (2014).
- [74] V. Goblot, A. Štrkalj, N. Pernet, J. L. Lado, C. Dorow, A. Lemaitre, L. Le Gratiet, A. Harouri, I. Sagnes, S. Ravets, A. Amo, J. Bloch, and O. Zilberberg, *Nat. Phys.* **16**, 832 (2020).
- [75] M. Reisner, Y. Tahmi, F. Piéchon, U. Kuhl, and F. Mortessagne, *Phys. Rev. B* **108**, 064210 (2023).
- [76] S. Franca, T. Seidemann, F. Hassler, J. van den Brink, and I. C. Fulga, *Phys. Rev. B* **109**, L241103 (2024).
- [77] A. Dareau, E. Levy, M. B. Aguilera, R. Bouganne, E. Akkermans, F. Gerbier, and J. Beugnon, *Phys. Rev. Lett.* **119**, 215304 (2017).
- [78] H. Huang, and F. Liu, *Phys. Rev. Lett.* **121**, 126401 (2018).
- [79] H. Huang, and F. Liu, *Phys. Rev. B* **100**, 085119 (2019).
- [80] R. Chen, C.-Z. Chen, J.-H. Gao, B. Zhou, and D.-H. Xu, *Phys. Rev. Lett.* **124**, 036803 (2020).
- [81] M. Kohmoto, *Phys. Rev. Lett.* **51**, 1198 (1983).
- [82] X.-J. Liu, Z.-X. Liu, and M. Cheng, *Phys. Rev. Lett.* **110**, 076401 (2013).
- [83] See Supplementary Material for more details.
- [84] B. Gadway, *Phys. Rev. A* **92**, 043606 (2015).
- [85] E. J. Meier, F. A. An, and B. Gadway, *Phys. Rev. A* **93**,

- 051602(R) (2016).
- [86] F. A. An, E. J. Meier, and B. Gadway, *Nat. Commun.* **8**, 325 (2017).
- [87] F. A. An, E. J. Meier, J. Ang'ong'a, and B. Gadway, *Phys. Rev. Lett.* **120**, 040407 (2018).
- [88] Y. Wang, J.-H. Zhang, Y. Li, J. Wu, W. Liu, F. Mei, Y. Hu, L. Xiao, J. Ma, C. Chin, and S. Jia, *Phys. Rev. Lett.* **129**, 103401 (2022).
- [89] Y. Li, J. Zhang, Y. Wang, H. Du, J. Wu, W. Liu, F. Mei, J. Ma, L. Xiao, and S. Jia, *Light. Sci. Appl.* **11**, 13 (2022).
- [90] Q. Liang, D. Xie, Z. Dong, H. Li, H. Li, B. Gadway, W. Yi, and B. Yan, *Phys. Rev. Lett.* **129**, 070401 (2022).
- [91] H. Li, Z. Dong, S. Longhi, Q. Liang, D. Xie, and B. Yan, *Phys. Rev. Lett.* **129**, 220403 (2022).
- [92] Y. Li, H. Du, Y. Wang, J. Liang, L. Xiao, W. Yi, J. Ma, and S. Jia, *Nat. Commun.* **14**, 7560 (2023).
- [93] Q. Liang, Z. Dong, J.-S. Pan, H. Wang, H. Li, Z. Yang, W. Yi, and B. Yan, *Nat. Phys.* **20**, 1738 (2024).
- [94] S. N. M. Paladugu, T. Chen, F. A. An, B. Yan, and B. Gadway, *Commun. Phys.* **7**, 39 (2024).
- [95] F. Cardano, A. D'Errico, A. Dauphin, M. Maffei, B. Piccirillo, C. de Lisio, G. De Filippis, V. Cataudella, E. Santamato, L. Marrucci, M. Lewenstein, and P. Massignan, *Nat. Commun.* **8**, 15516 (2017).
- [96] B. Zhou, C. Yang, and S. Chen, *Phys. Rev. B* **100**, 184313 (2019).
- [97] B. Zhou, Y. Zeng, and S. Chen, *Phys. Rev. B* **104**, 094311 (2021).
- [98] M. Sadrzadeh, R. Jafari, and A. Langari, *Phys. Rev. B* **103**, 144305 (2021).
- [99] R. Nehra, and D. Roy, *Phys. Rev. B* **109**, 094311 (2024).
- [100] H.-X. Xiao, W. Jiang, P. Qian, H. Li, Z. Li, H. Shen, and B. Chen, *Phys. Rev. B* **110**, 064306 (2024).
- [101] Y. Jing, J.-J. Dong, Y.-Y. Zhang, and Z.-X. Hu, *Phys. Rev. Lett.* **132**, 220402 (2024).
- [102] M. Heyl, A. Polkovnikov, and S. Kehrein, *Phys. Rev. Lett.* **110**, 135704 (2013).
- [103] M. Heyl, *Phys. Rev. Lett.* **113**, 205701 (2014).
- [104] M. Heyl, *Phys. Rev. Lett.* **115**, 140602 (2015).
- [105] R. Jafari, and H. Johannesson, *Phys. Rev. Lett.* **118**, 015701 (2017).
- [106] M. Heyl, F. Pollmann, and B. Dóra, *Phys. Rev. Lett.* **121**, 016801 (2018).
- [107] X. N, B.-B. W, X. Chen, Z. Zhang, X. Zhao, C. Qiu, Y. Tian, Y. Ji, T. Xin, D. Lu, and J. Li, *Phys. Rev. Lett.* **124**, 250601 (2020).
- [108] S. Bandyopadhyay, A. Polkovnikov, and A. Dutta, *Phys. Rev. Lett.* **126**, 200602 (2021).
- [109] U. Schneider, L. Hackermüller, J. P. Ronzheimer, S. Will, S. Braun, T. Best, I. Bloch, E. Demler, S. Mandt, D. Rasch, and A. Rosch, *Nat. Phys.* **8**, 213 (2012).
- [110] H. P. Lüschen, S. Scherg, T. Kohlert, M. Schreiber, P. Bordia, X. Li, S. Das Sarma, and I. Bloch, *Phys. Rev. Lett.* **120**, 160404 (2018).
- [111] Y. Wang, L. Zhang, S. Niu, D. Yu, and X.-J. Liu, *Phys. Rev. Lett.* **125**, 073204 (2020).

## Supplementary Materials for "Fibonacci-Modulation-Induced Multiple Topological Anderson Insulators"

This Supplementary Material provides detailed explanations of the scattering-matrix method used to calculate the  $\mathcal{Z}_2$  topological quantum number  $Q$ , the derivation of topological phase boundaries, an analysis of an off-diagonal Fibonacci-modulated SOC chain, and the experimental realization.

### I. SCATTERING-MATRIX METHOD

To determine the topological properties of the quasiperiodic-modulated SOC chain, we utilize the scattering matrix  $S$ , which relates the incoming and outgoing wave amplitudes at the Fermi level [1]:

$$S = \begin{pmatrix} \tilde{R}_{\leftarrow} & \tilde{T}_{\leftarrow} \\ \tilde{T}_{\rightarrow} & \tilde{R}_{\rightarrow} \end{pmatrix}, \quad (\text{S1})$$

where  $\tilde{R}_{\leftarrow}$  and  $\tilde{R}_{\rightarrow}$  are  $2 \times 2$  reflection matrices at the left and right ends of the chain, respectively, while  $\tilde{T}_{\leftarrow}$  and  $\tilde{T}_{\rightarrow}$  are the corresponding transmission matrices. The  $\mathcal{Z}_2$  topological quantum number  $Q$  is defined as:

$$Q = \text{sgn} \left[ \text{Det} \left( \tilde{R}_{\leftarrow} \right) \right] = \text{sgn} \left[ \text{Det} \left( \tilde{R}_{\rightarrow} \right) \right], \quad (\text{S2})$$

where  $\text{sgn}[\dots]$  denotes the sign function. A value of  $Q = 1$  indicates a topologically trivial phase, while  $Q = -1$  signifies a topologically nontrivial phase. To account for the effects of disorder, we define the disorder-averaged topological invariant  $\bar{Q}$ , calculated over  $N_c$  disorder realizations. In our analysis,  $N_c$  configurations are sampled for different values of  $\phi \in [0, 2\pi]$ .

The scattering matrix can be derived using the transfer-matrix scheme. Based on the Hamiltonian given in Eq. (1) of the main text, the zero-energy Schrödinger equation leads to the following recursive relation:

$$\begin{pmatrix} \mathcal{R}_{i+1,i}^\dagger \Psi_i \\ \Psi_{i+1} \end{pmatrix} = \tilde{B}_i \begin{pmatrix} \mathcal{R}_{i,i-1}^\dagger \Psi_{i-1} \\ \Psi_i \end{pmatrix} \quad (\text{S3})$$

where

$$\tilde{B}_i = \begin{pmatrix} 0 & \mathcal{R}_{i+1,i}^\dagger \\ -\mathcal{R}_{i,i+1}^{-1} & -\mathcal{R}_{i,i+1}^{-1} \mathcal{U}_i \end{pmatrix}. \quad (\text{S4})$$

The relation indicates that wave amplitudes at the two ends of the chain ( $i = 1$  and  $i = N$ ) are connected by the total transfer matrix  $\tilde{B} = \tilde{B}_L \tilde{B}_{L-1} \dots \tilde{B}_1$ . To separate the right-moving and left-moving waves into the upper and lower four components, we transform the transfer matrix using the basis rotation:

$$B_i = U^\dagger \tilde{B}_i U, \quad (\text{S5})$$

where

$$U = \frac{1}{\sqrt{2}} \begin{pmatrix} I & I \\ iI & -iI \end{pmatrix}, \quad (\text{S6})$$

and  $I$  is a  $2 \times 2$  identity matrix. In this base, the reflection ( $\tilde{R}_{\leftarrow}, \tilde{R}_{\rightarrow}$ ) and transmission ( $\tilde{T}_{\leftarrow}, \tilde{T}_{\rightarrow}$ ) matrices can be determined via the relations:

$$\begin{pmatrix} \tilde{T}_{\rightarrow} \\ 0 \end{pmatrix} = B \begin{pmatrix} I \\ \tilde{R}_{\leftarrow} \end{pmatrix}, \quad \begin{pmatrix} \tilde{R}_{\rightarrow} \\ I \end{pmatrix} = B \begin{pmatrix} 0 \\ \tilde{T}_{\leftarrow} \end{pmatrix}, \quad (\text{S7})$$

where  $B = B_L B_{L-1} \dots B_1$ .



## II. DERIVATION OF TOPOLOGICAL PHASE BOUNDARIES

In the topologically nontrivial regime, the zero edge modes emerge with a finite localization length. Conversely, in the trivial regime, these edge modes disappear, giving way to bulk states characterized by a divergence in localization length. To analytically determine the topological phase boundaries, we examine the localization length of the zero modes. The zero mode Schrödinger equation for the Fibonacci-modulated model,  $H|\Psi\rangle = 0$ , is expressed as:

$$-t_0(\psi_{i+1\uparrow} + \psi_{i-1\uparrow}) + t_{so}(\psi_{i+1\downarrow} - \psi_{i-1\downarrow}) + U_i\psi_{i\uparrow} = 0, \quad (\text{S8})$$

$$t_0(\psi_{i+1\downarrow} + \psi_{i-1\downarrow}) + t_{so}(\psi_{i-1\uparrow} - \psi_{i+1\uparrow}) - U_i\psi_{i\downarrow} = 0, \quad (\text{S9})$$

where  $\psi_{i\beta}$  represents the probability amplitude of the zero mode for spin  $\beta = \{\uparrow, \downarrow\}$  at the  $i$ th lattice, and  $U_i = [\lambda \text{sgn}(\cos(2\pi\alpha i + \phi) - \cos(\pi\alpha)) + M]$ . Applying a local transformation  $\phi_i^+ = \psi_{i\uparrow} + \psi_{i\downarrow}$  and  $\phi_i^- = \psi_{i\uparrow} - \psi_{i\downarrow}$  [2], the equation decouple into two independent equations of similar form:

$$-t_0(\phi_{i+1}^- + \phi_{i-1}^-) + t_{so}(\phi_{i-1}^- - \phi_{i+1}^-) + U_i\phi_i^- = 0, \quad (\text{S10})$$

$$-t_0(\phi_{i+1}^+ + \phi_{i-1}^+) + t_{so}(\phi_{i+1}^+ - \phi_{i-1}^+) + U_i\phi_i^+ = 0. \quad (\text{S11})$$

Focusing on one decoupled equation, the evolution can be written in terms of the transfer matrix:

$$\begin{pmatrix} \phi_{i+1}^- \\ \phi_i^- \end{pmatrix} = T_i \begin{pmatrix} \phi_i^- \\ \phi_{i-1}^- \end{pmatrix} \quad (\text{S12})$$

where the transfer matrix  $T_i$  is:

$$T_i = \begin{pmatrix} \frac{U_i}{t_0+t_{so}} & \frac{t_{so}-t_0}{t_0+t_{so}} \\ 1 & 0 \end{pmatrix}. \quad (\text{S13})$$

The localization length  $\tilde{\lambda}$  of the zero modes is then determined by

$$\tilde{\lambda}^{-1} = \lim_{L \rightarrow \infty} \frac{1}{L} \ln \|T\|, \quad (\text{S14})$$

where  $\|\cdot\|$  denotes the norm of the matrix, and  $T \equiv \prod_{i=1}^L T_i$  is the total transfer matrix. The divergence of the localization length  $\tilde{\lambda}$ , i.e.,  $\tilde{\lambda} \rightarrow \infty$ , identifies the topological phase boundaries, which satisfy the condition:

$$|\text{Tr}(T)| - \text{Det}(T) = 1. \quad (\text{S15})$$

## III. OFF-DIAGONAL-FIBONACCI-MODULATED SOC CHAIN

In this section, we examine an off-diagonal Fibonacci-modulated SOC chain, described by the Hamiltonian (1) in the main text with  $\mathcal{U}_i = M\sigma_z$  and

$$\mathcal{R}_{ij} = - \left[ t_0 - \frac{\Delta}{2} \text{sgn}[\cos(2\pi\alpha i + \phi) - \cos(\pi\alpha)] + \frac{\Delta}{2} \right] \sigma_z \pm it_{so}\sigma_y, \quad (\text{S16})$$

where the  $\pm$  corresponds to the hopping along the  $\pm\hat{x}$  direction. The diagonal terms of  $\mathcal{R}$  describe the spin-conserved hopping with the amplitude  $t_0$ , modulated by the Fibonacci sequence with strength  $\Delta$ . The off-diagonal terms represent spin-flip hopping between nearest neighbors with an amplitude  $\mathcal{R}$ . We set  $t_0 = 1$  as the unit of energy throughout this discussion.

We calculated the topological phase diagram in the  $\Delta - M$  plane, as shown in Fig. S1(a), using  $L = 610$ ,  $t_{so} = 0.25$ , and  $N_c = 50$  disorder realizations. The dashed lines represent the topological phase boundaries, numerically determined by the condition  $|\text{Tr}(T)| - \text{Det}(T) = 1$ , where  $T = \prod_{i=1}^L T_i$  and

$$T_i = \begin{pmatrix} \frac{M}{\xi_i^{(+)}} & \frac{\xi_{i-1}^{(-)}}{\xi_i^{(+)}} \\ 1 & 0 \end{pmatrix}. \quad (\text{S17})$$

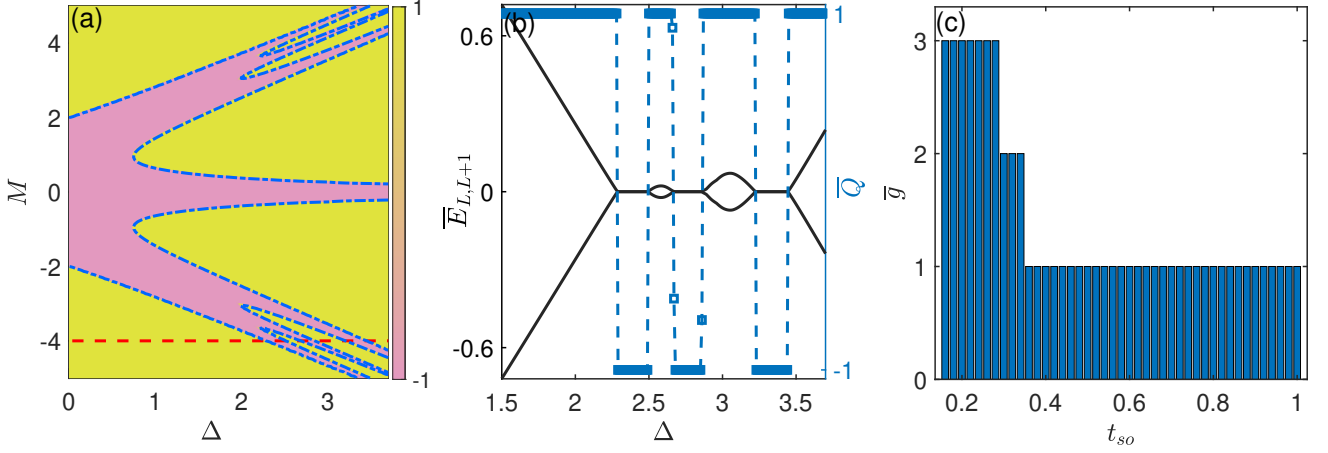


FIG. S1. (a) Topological phase diagram of an off-diagonal-Fibonacci-modulated SOC chain in  $\Delta - M$  plane with  $L = 610$ ,  $\alpha = F_{13}/F_{14}$ , and  $t_{so} = 0.25$ . The blue dashed lines represent the topological phase boundaries numerically obtained by Eq. (S15). (b) Two disorder-averaged energies  $\bar{E}_L$  and  $\bar{E}_{L+1}$  at the center of the spectrum and the disorder-averaged topological number  $\bar{Q}$  as a function of  $\Delta$  under OBC with  $t_{so} = 0.25$  and  $M = -4$ . (c) The number of times that the TAI phase emerges as a function of  $t_{so}$  with  $M = -4$ . Here, all the data are averaged by  $N_c = 50$  disorder realizations.

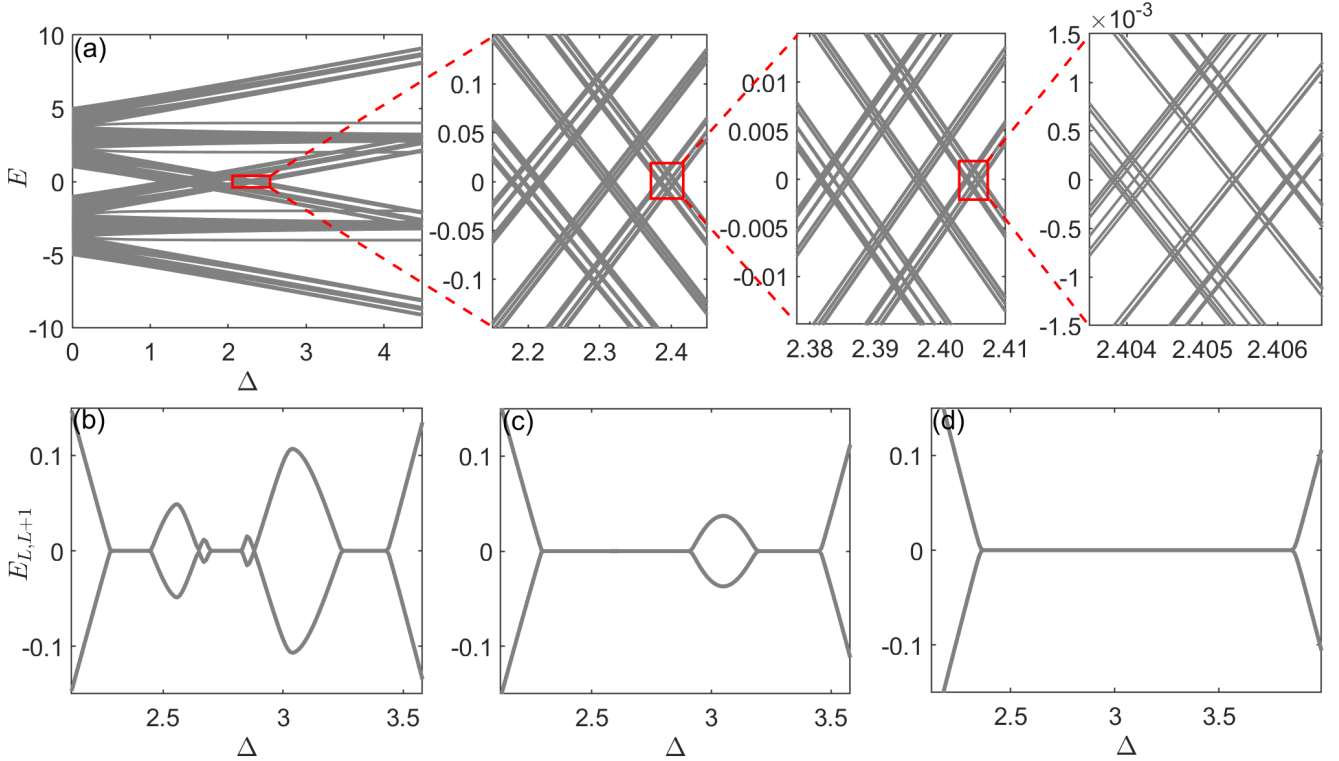


FIG. S2. (a) Self-similarities of energy spectrum as a function of  $\Delta$  with  $t_{so} = 0$ . Two central energy levels  $E_L$  and  $E_{L+1}$  as a function of  $\Delta$  with (b)  $t_{so} = 0.2$ , (c) 0.3, and (d) 0.9. Here,  $M = -4$ ,  $\phi = 0$ , and  $L = 610$ .

where,  $\xi_i^{(\pm)} = t_{so} \pm [t_0 - \frac{\Delta}{2} \text{sgn}[\cos(2\pi\alpha i + \phi) - \cos(\pi\alpha)] + \frac{\Delta}{2}]$ . The results show that the topologically nontrivial phase is robust against weak modulation for  $0 < \Delta < 2$  but transitions to a trivial phase as the modulation strength increases. Notably, when  $M = 0$ , the system remains in the topological phase regardless of  $\Delta$ . For  $2 < |M| < 3.05$ , the system undergoes a topological phase transition from trivial to nontrivial and back to trivial with increasing  $\Delta$ , demonstrating the emergence of the TAI phase. When  $|M| \geq 3.05$ , the system exhibits multiple transitions into the TAI phase before ultimately reverting to a trivial phase at higher  $\Delta$ . Figure S1(b) shows the disorder-averaged

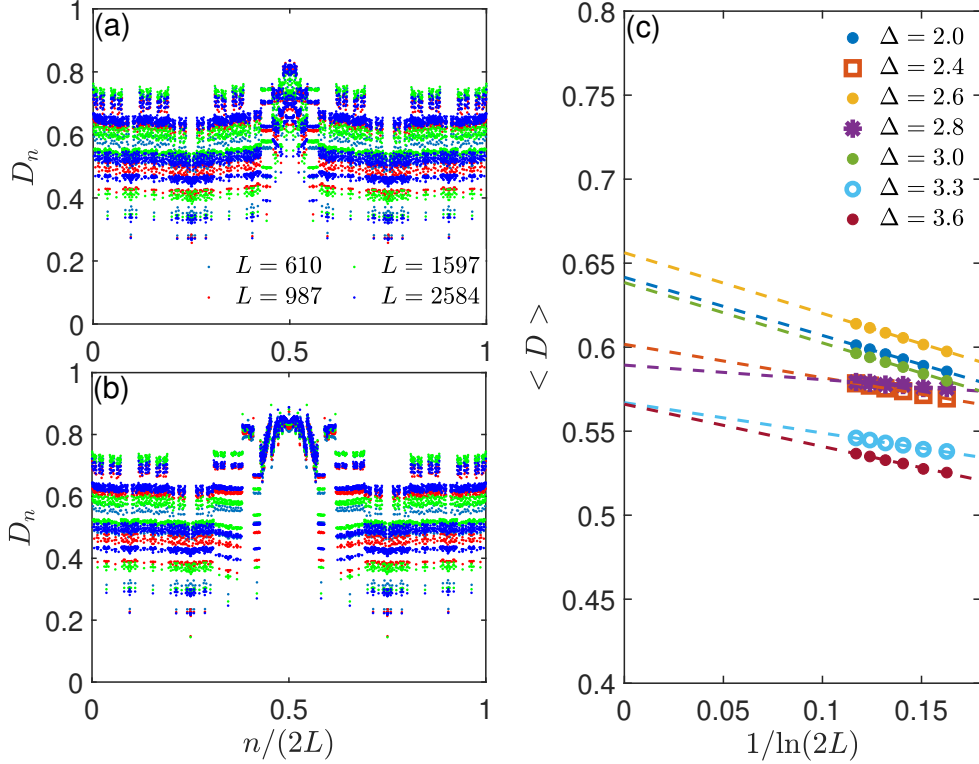


FIG. S3. Fractal dimensions  $D_n$  for different system sizes under PBC for (a)  $\Delta = 2.4$  and (b)  $\Delta = 3$ , respectively. (c) The scaling of the mean fractal dimensions  $\langle D \rangle$  for various  $\Delta$  values. Here,  $t_{so} = 0.25$ ,  $M = -4$ , and  $\phi = 0$ .

energies of the two center modes,  $\bar{E}_L$  and  $\bar{E}_{L+1}$ , alongside the  $\mathbb{Z}_2$  topological number  $\bar{Q}$  as a function of the modulation strength  $\Delta$ , with  $M = -4$  and  $t_{so} = 0.25$ . The results indicate that the moderate modulation  $\Delta$  induces changes in the nontrivial invariant within the regions  $\Delta \in [2.28, 2.49] \cup [2.66, 2.86] \cup [3.22, 3.44]$ , where disorder-averaged zero modes are also observed. For  $\Delta > 3.44$ , the TAI phase vanishes. In Fig. S1(c), we show the number of times the TAI phase emerges,  $\bar{\gamma}$ , as a function of  $t_{so}$  for  $M = -4$ . Similar to the on-site modulated case,  $\bar{\gamma}$  in the off-diagonal-modulated case increases as  $t_{so}$  decreases. To understand this phenomenon, we numerically calculate the energy spectrum of two decoupled off-diagonal-Fibonacci-modulated chains without the SOC term ( $t_{so} = 0$ ) as a function of  $\Delta$ , shown in Fig. S2(a) for  $M = -4$  and  $\phi = 0$ . Within the range  $\Delta \in (1.16, 2.41)$ , the middle bands overlap, forming three distinct clusters of band-crossing regions separated by two band gaps near zero energy. These clusters further split into sub-clusters, creating a self-similar fractal structure in the thermodynamic limit, as seen in Fig. S2(a). As the SOC strength  $t_{so}$  increases, these band gaps, with magnitudes comparable to  $t_{so}$ , progressively close and reopen, leading to the emergence of nontrivial zero-energy modes in these gaps, as depicted in Fig. S2(b). This suggests an infinite number of TAI phases emerge in the small  $t_{so}$  limit and in the thermodynamic limit, forming a topologically fractal structure. As  $t_{so}$  increases further, adjacent topologically nontrivial regions merge, reducing the number of distinct TAI phases, as illustrated in Figs. S2(b) and S2(c). These findings confirm that an off-diagonal Fibonacci-modulated SOC chain supports multiple TAI phases, with their occurrence strongly dependent on  $t_{so}$ .

Figures S3(a) and S3(b) show the fractal dimensions for different system sizes under periodic boundary condition (PBC) with  $\phi = 0$  for  $\Delta = 2.4$  and  $\Delta = 3$ , respectively. For both topologically trivial and nontrivial phases, the fractal dimensions of nearly all states are system-size independent, deviating from the extremes of 0 and 1. The scaling behavior of the mean fractal dimension  $\langle D \rangle$  for various  $\Delta$  values, in both topologically trivial ( $\Delta = 2.4, 2.8,$  and  $3.3$ ) and nontrivial ( $\Delta = 2, 2.6, 3,$  and  $3.6$ ) phases, is shown in Fig. S3(c). In the thermodynamic limit,  $\langle D \rangle$  approaches values that deviate from both 0 and 1 in both phases. Our results suggest that the emergence of the TAI phase does not affect the localization properties of the system, and the states remain multifractal.

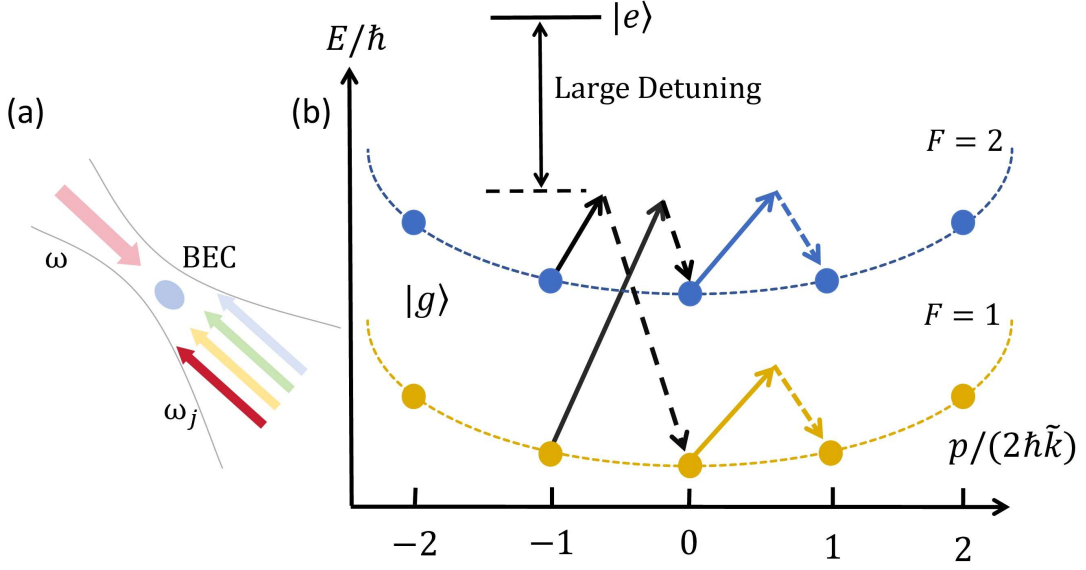


FIG. S4. Illustration of experimental scheme. (a) A quasi-1D BEC is illuminated by a pair of counterpropagating laser beams: one with a fixed frequency  $\omega$  and the other containing multifrequency components  $\omega_j$ . (b) The lasers, far detuned from the atomic transition, drive a series of engineered two-photon Bragg transitions. These transitions couple different momentum states within the same ground-state hyperfine manifold (blue and yellow arrows) or across different ground-state hyperfine manifolds (black arrows), with an increment of  $2\hbar\tilde{k}$ , where  $\tilde{k} = 2\pi/\tilde{\lambda}$  with  $\tilde{\lambda}$  being the wave length of the lasers. The solid and dashed arrows represent the processes of photon absorption and emission, respectively.

#### IV. EXPERIMENTAL REALIZATION

Our Fibonacci-modulated SOC model can be implemented along the momentum lattice in a cold atom system using a Bose-Einstein condensate (BEC), as illustrated in Fig. S4. In this setup, the spin and lattice-site degrees of freedom are encoded in the two ground-state hyperfine manifolds of selected atoms, such as  $^{87}\text{Rb}$  [3]. Specifically, the hyperfine state  $F = 1$  represents spin-down, while  $F = 2$  represents spin-up. A pair of counter-propagating laser beams is employed: the incoming laser beam has a fixed frequency, while the acousto-optic modulator in the reflected laser beam generate multi-frequency components. These laser beams drive a series of two-photon Bragg transitions between adjacent discrete momentum states. Transitions within the same hyperfine manifold enable nearest-neighbor couplings with the same spin, corresponding to the diagonal terms of  $R$ . In contrast, transitions between different hyperfine manifolds facilitate nearest-neighbor couplings with opposite spins, corresponding to the off-diagonal terms of  $R$ . By precisely adjusting the amplitude of each multi-frequency component, all couplings can be individually controlled. Additionally, the on-site potentials  $\mathcal{U}_i$  can be tuned via the detuning of the two-photon Bragg transitions.

[1] P. Zhang and F. Nori, *New J. Phys.* **18**, 043033 (2016).

[2] Y. Wang, L. Zhang, S. Niu, D. Yu, and X.-J. Liu, *Phys. Rev. Lett.* **125**, 073204 (2020).

[3] Q. Liang, Z. Dong, J.-S. Pan, H. Wang, H. Li, Z. Yang, W. Yi, and B. Yan, *Nat. Phys.* **20**, 1738 (2024).